Electrochimica Acta 557 (2026) 148494

Contents lists available at ScienceDirect

Electrochimica Acta

journal homepage: www.journals.elsevier.com/electrochimica-acta

Microbial electrosynthesis for CO_2 conversion: Process limiting steps investigated by micro-scale modeling

V. Murugesan, Remco Hartkamp, Johan T. Padding *

Complex Fluid Processing, Process & Energy Department, Delft University of Technology, Leeghwaterstraat 39, 2628 CB, Delft, The Netherlands
e-Refinery Institute, Delft University of Technology, Leeghwaterstraat 39, 2628 CB, Delft, The Netherlands
Process & Product Technology Institute (Pro2Tech), Delft University of Technology, Leeghwaterstraat 39, 2628 CB, Delft, The Netherlands

ARTICLE INFO

Keywords:
Bio-electrochemical systems
Mass transport
Microbe-scale model
Biofilm thickness
Caproate selectivity
Mediated electron transfer (MET)

ABSTRACT

The advancement of microbial electrosynthesis systems (MES) towards industrialization is currently hindered by a limited understanding of the fundamental constraints affecting selective production of high-value chemicals. To address this challenge, we develop a comprehensive computational model that integrates microbial, electrochemical, and acid–base reactions with pore-scale transport processes within a three-dimensionally resolved biofilm. This study investigates the H_2-mediated CO_2 fixation pathway to acetate, butyrate, and caproate. The effect of applied cathode potential and biofilm thickness on macroscopic parameters, such as efficiency and selectivity, is analyzed based on local concentrations and electrochemical and biochemical fluxes. Among the limiting factors, the availability of CO_2 emerges as the main limitation for biochemical reactions due to its low solubility and high half-saturation constant. Additionally, hydrogen – serving as the electron mediator – limits the reaction rate at low current densities and reduces electron transfer efficiency at higher current densities. A key insight from our study is the identification of an optimal electrode potential for each biofilm thickness, balancing both H_2 transfer and CO_2 consumption efficiencies. Furthermore, carbon selectivity shifts with increasing biofilm thickness: net acetate production declines while caproate production increases. This trend is attributed to the prolonged residence time of metabolic intermediates within thicker biofilms, promoting chain elongation pathways. Thus, our work takes an important step towards a fundamental understanding of caproate selectivity across different biofilms, which can be used to optimize the electrode structure and operating conditions to control the local biofilm thickness.

1. Introduction

The atmospheric concentration of CO_2 has reached alarming levels, primarily due to the continued reliance on fossil fuels [1,2]. In response, significant efforts have been directed towards mitigating excess CO_2 emissions, including approaches such as carbon capture and utilization (CCU) [3–5]. Microbial electrosynthesis (MES) provides a promising utilization approach, by using electricity to convert CO_2 into acetate and other useful organic compounds [3,6]. This technology leverages the ability of microorganisms to transfer electrons and convert CO_2 into multicarbon products through intracellular metabolic pathways. MES offers several benefits over other CO_2 conversion techniques, such as the ability of biocatalysts to self-regenerate, mild operating conditions, the absence of toxic reagents, and environmental sustainability. These benefits make MES an attractive and promising method for CO_2 conversion [7–9].

MES employs pure or mixed cultures of microorganisms that can take up electrons from the electrode through conductive pili (direct electron transfer, DET) or utilize dissolved electron carriers (mediated electrochemical electron transfer, MET) produced at the electrode to reduce CO_2 [10,11]. Since the first proof of concept by Nevin et al. [12] in 2010, MES has been actively studied for the production of acetate and for synthesizing higher-value compounds, such as butyrate and caproate, through chain elongation. Thus far, most research on MES has been focused on studying the electron transfer mechanism, metabolic routes to reduce CO_2, improving and understanding microbial strains, and enhancing the electrode structure and material [3,4,13,14]. Despite significant achievements on these fronts, MES has yet to achieve industrial viability [3,15]. Reaching this goal requires a deeper understanding of the rate-limiting steps, identification of optimal operating conditions, and development of a scale-up strategy that integrates

* Corresponding author at: Complex Fluid Processing, Process & Energy Department, Delft University of Technology, Leeghwaterstraat 39, 2628 CB, Delft, The Netherlands.
E-mail addresses: v.murugesan@tudelft.nl (V. Murugesan), r.m.hartkamp@tudelft.nl (R. Hartkamp), J.T.Padding@tudelft.nl (J.T. Padding).

https://doi.org/10.1016/j.electacta.2026.148494
Received 4 November 2025; Received in revised form 17 February 2026; Accepted 18 February 2026
Available online 19 February 2026

electrochemical and biochemical processes while managing their concurrent physical, chemical, and biological interactions. To that end, as noted by Korth et al. [16], computational modeling is essential to obtain a detailed understanding of MES systems by decoupling these interactions across length scales, enabling systematic analysis and optimization.

Several modeling studies have advanced our understanding of MES bioelectrochemistry. Kazemi et al. [17] developed a 1D cathode–biofilm model based on Nernst–Monod kinetics, capturing diffusion-driven substrate and product transport while neglecting electromigration. Gadkari et al. [18] proposed a dynamic model including both chambers to analyze the influence of substrate concentrations and operation cycles on efficiency. Cabau-Peinado et al. [13] introduced a black-box kinetic model for acetate, butyrate, and caproate production, highlighting the limitation of dissolved CO_2 and estimating kinetic parameters for a mediator-based MET pathway. Kim et al. [19] presented a fundamental model of acetate production via direct electron transfer, accounting for biofilm growth in porous electrodes. Beyond acetate and carboxylates, Li et al. [20] modeled methane-producing MES, incorporating diffusion-driven transport and local pH effects, while Gharbi et al. [21] extended this to dynamic systems with pH inhibition.

Acetate is the predominant product in most MES cells, but efforts have been made to promote the production of higher-value compounds such as caproate [22]. Consequently, several experimental studies have focused on enhancing the caproate production by varying the CO_2 loading rate, increasing the hydraulic retention time, and supplying the precursors for caproate [22,23]. Previous numerical studies focused on either methane or acetate production, while numerical simulations towards chain elongation are essential to identify the governing transport and reaction limitations that determine caproate selectivity and yield. Moreover, the effect on bioelectrochemical processes with MET using H_2 has not been understood at the biofilm level, as most studies have focused on DET. However, DET prevails at low cathodic potential, which limits the achievable current densities [9,24]. In contrast, H_2-mediated electron transfer is the rapid way of transferring electrons to the microbes for higher production rates [24]. Moreover, the electrochemically produced H_2 that facilitates MET in MES has enabled higher production rates of longer-chain carboxylates such as butyrate [25]. Studies have shown that *Sporomusa sp.*, which is an anaerobic strain, can reduce CO_2 through a chain elongation pathway, with the use of H_2 [17,26,27].

Building on the works that improved caproate yield, this study will account for the acetate production as well as the chain elongation process by MET through H_2. The concentration gradients across the biofilm can be modulated by the pH, electric field, and the concentration of buffer compounds in the electrolyte. Understanding these gradients is crucial for optimizing MES performance and scaling up, as the operating current density and production rates continue to increase [3]. Previous (one-dimensional) modeling studies relied on assumed effective diffusivities, as the biofilm structure was not explicitly resolved. This approach introduces uncertainty when three-dimensional data are unavailable. To address this limitation, we implement a resolved microbe-scale model in which the biofilm is explicitly represented. This eliminates the need for assumed effective parameters and instead allows transport behavior to emerge naturally from the simulated biofilm domain (Differences between our resolved model and a homogeneous model are shown in Supplementary information S12). Our numerical model incorporates species transport by both diffusion and migration in a resolved microbe-scale biofilm that can fix CO_2 to produce long-chain carboxylates up to caproate. The biofilm is represented by randomly packed spherocylinders (with uniform biomass density) with the characteristic size of the *Sporomusa ovata* on top of an electrode. We begin by validating that our transport model and the corresponding carboxylate product ratios accurately reproduce previously reported values. We then offer detailed insights that extend and complement existing data.

The main objective of this work is to study the complex interplay between the electrochemical, biochemical, and homogeneous acid–base reactions that regulate the local pH. The complex nature of MES, involving multiple interactions that influence performance and chain length, is examined through the effects of cathode potential and biofilm thickness. Reactor-scale parameters, such as H_2 transfer and CO_2 utilization efficiencies, as well as product selectivity, are analyzed over a range of cathode potentials and biofilm thicknesses (BFT). Finally, the transport and reaction limitations are discussed by analyzing the local species concentrations and connecting them to the reactor-scale results.

2. Model description

An MES system consists of anodic and cathodic chambers separated by a proton exchange membrane to enable selective ion transport and avoid product crossover [28]. In the cathodic chamber, microbes are either attached to the cathode to form a biofilm or remain planktonic in the catholyte. These anaerobic bacteria serve as a catalyst to fix CO_2 to produce the carboxylates. There are several strains of bacteria that can perform these bioconversions; however, the specific strains responsible for different pathways remain unclear. For simplicity, a black box kinetic model is used for biochemical reactions, according to which, the biofilm is considered to be composed of only *Sporomusa ovata*, each of which has a spherocylindrical shape with a size of approximately 10 × 1 μm. In a 3D porous electrode, such as graphite felt, the microbes may form internal and external biofilms [3]. For this micro-scale study, we focus on the external biofilm, which directly interfaces with the bulk electrolyte, due to its large thickness relative to internal biofilm within the felt, also represents critical transport resistance for substrate supply and product removal. A schematic representation of the biofilm system is shown in Fig. 1b. The system is composed of the cathode surface, the biofilm, and, in its vicinity is the diffusion boundary layer. The continuous concentration and electrolyte potential fields are solved only in the extracellular electrolyte phase between microbial cells. In Fig. 1c, the potential difference applied over the system drives the hydrogen evolution reaction (HER) at the cathode (Γ_e). CO_2 diffuses from the bulk across the diffusion boundary layer to be reduced within the biofilm, along with the electrochemically produced H_2. The consumption of substrates and production of carboxylates is modeled as surface fluxes at the microbe-electrolyte interface (Γ_b). Γ_o represents the outer boundary, which covers a fraction of the diffusion boundary layer from the vicinity of the biofilm. A 3D structure of the biofilm in Fig. 1 was generated with randomly arranged microbes. For computational efficiency, the domain is periodic in the lateral directions (X and Y directions). All the simulations were performed using COMSOL Multiphysics Version 6.2.

The governing equations for the electrolyte phase (grey zone in Fig. 1c) and the different interfaces in the system are further formulated and discussed in detail based on the following assumptions and simplifications. (**1**) The biofilm is well-developed, resulting in a biofilm with tightly packed microbes. There are no planktonic microbes in the catholyte. (**2**) The biofilm is composed of a single strain of densely packed bacteria that can perform acetogenesis and chain-elongation to butyrate and caproate. (**3**) The temperature of the system is strictly controlled. (**4**) The microbial growth rate is negligible compared to the rate of chemical reactions and their corresponding transport in this micro-scale system (Supplementary information S3). (**5**) Therefore, a static biofilm is considered with homogeneous biomass density and random cell orientation. (**6**) The effect of pH on the biochemical reaction rates is unknown, and hence it is neglected in this model. (**7**) The microbes cannot directly take up electrons from the cathode. (**8**) Intracellular transport and electron transfer pathways are not resolved explicitly. Microbial metabolism is represented through surface-based reaction fluxes imposed at the microbe–electrolyte interface (Γ_b). (**9**)

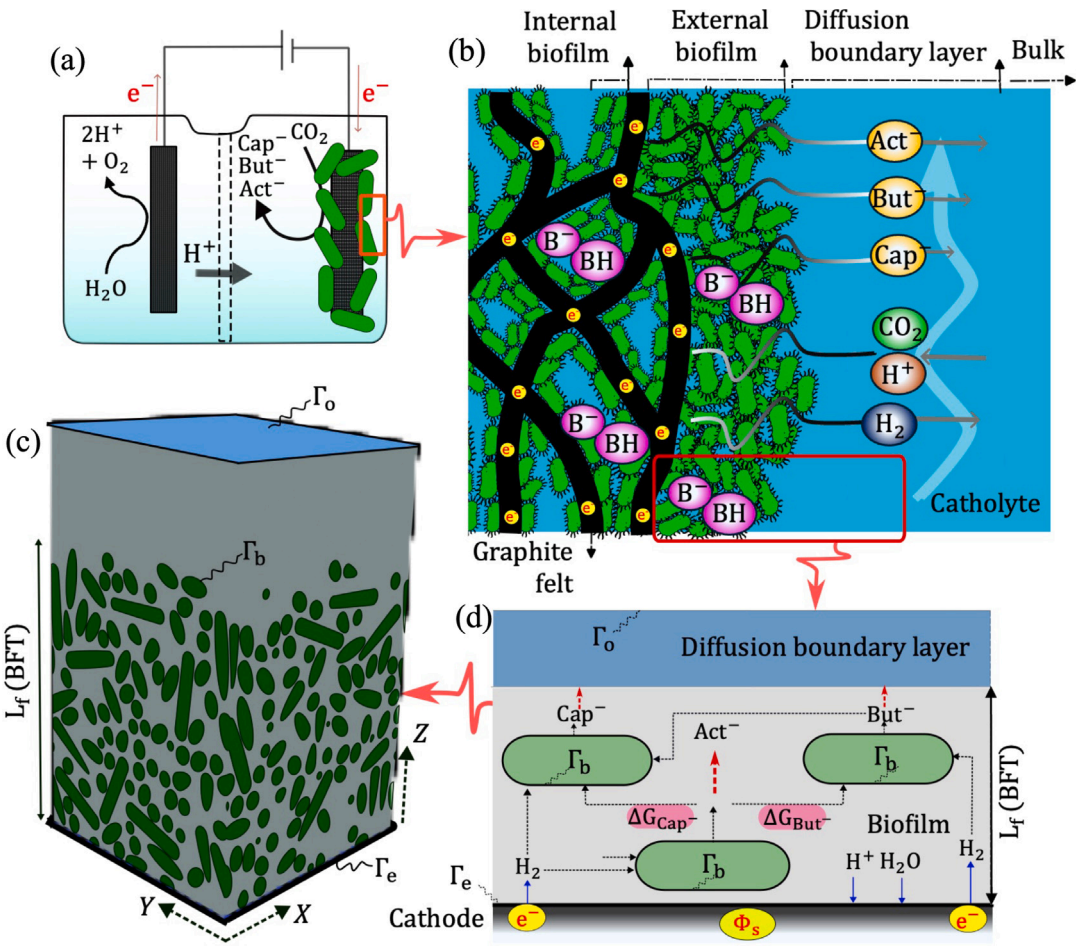

Fig. 1. Schematic representation of the species source at different interfaces. The domain considered in the model encompasses the biofilm and diffusion boundary layer. The interface between the electrode and electrolyte is Γ_e and Γ_b is the microbe-electrolyte interface. Γ_o represents the exit boundary, which is assumed to be a plane within the diffusion boundary layer (starting from L_f and ending at L_d).

Since the pH across the biofilm increases towards the electrode surface with respect to the bulk at pH=5.8, which is higher than the pKa of the fatty acids, it is assumed they exist only in their conjugate base form. (**10**) CO_2 is the only inlet carbon source considered in this study. (**11**) Gas evolution, such as that of gaseous hydrogen, is not considered.

2.1. Biochemical reactions

In MES for the production of long-chain fatty acids, acetate is produced by fixing CO_2 through the acetyl-CoA (acetogenesis), famously known as the Wood–Ljungdahl metabolic pathway [5,29–32]. The chain elongation of acetate to butyrate and caproate can occur through multiple pathways [33]. One such pathway is reverse β-oxidation, which uses acetate and ethanol produced during solventogenesis [34,35]. The biochemical reactions can be modeled as multiple separate steps, such as the energy-providing catabolic reaction, the anabolic reaction for biomass production, the chain elongation reactions, and intracellular redox reactions (between NADH/NAD^+ and outer cytochromes) [13,22,36]. For the biochemical process, a black box model is used that encompasses all the major metabolic processes proposed by Cabau-Peinado et al. [13]. The acetogenesis reaction (catabolic reaction that yields energy), which is mediated through H_2, is given by [29,37]:

$$2\,CO_2 + 4\,H_2 \longrightarrow C_2H_3O_2^- + H^+ + 2\,H_2O \tag{1}$$

This work uses a CO_2-independent chain elongation pathway not linked to microbial growth, eventually eliminating the intermediates like ethanol [13]. The energy-demanding chain elongation reactions to butyrate and caproate mediated by H_2 are given by:

$$2\,C_2H_3O_2^- + 2\,H_2 + H^+ \longrightarrow C_4H_7O_2^- + 2\,H_2O, \tag{2}$$

$$C_2H_3O_2^- + C_4H_7O_2^- + 2\,H_2 + H^+ \longrightarrow C_6H_{11}O_2^- + 2\,H_2O\cdot \tag{3}$$

The Herbert–Pirt relation couples substrate (CO_2) uptake, biomass growth, and the elongation reactions to estimate the biochemical rates, but for the small system that is considered in this study, it is possible to decouple the biomass growth from the other reactions (**supplementary information S3**). Hence, the simplified form of the Herbert–Pirt relation is given by:

$$Q_i = \nu_i^{\mathrm{Act}} q_{\mathrm{Act}^-} + \nu_i^{\mathrm{But}} q_{\mathrm{But}} + \nu_i^{\mathrm{Cap}} q_{\mathrm{Cap}}, \tag{4}$$

with stoichiometric coefficients for acetogenesis, butyrate, and caproate elongation (ν_i^{Act}), (ν_i^{But}), and (ν_i^{Cap}) respectively. The respective local reaction rates (q_{Act^-}, q_{But^-}, q_{Cap^-}) are determined by the Michaelis–Menten equations given by:

$$q_{\mathrm{Act}^-} = q_{\mathrm{Act}^-}^{\max} \frac{C_{CO_2}}{C_{CO_2} + K_{CO_2}} \frac{C_{H_2}}{C_{H_2} + K_{H_2}}, \tag{5}$$

$$q_{\mathrm{But}} = q_{\mathrm{But}}^{\max} \frac{C_{\mathrm{Act}}}{C_{\mathrm{Act}} + K_{\mathrm{Act}}} \frac{C_{H_2}}{C_{H_2} + K_{H_2}}, \tag{6}$$

$$q_{\mathrm{Cap}} = q_{\mathrm{Cap}}^{\max} \frac{C_{\mathrm{Act}}}{C_{\mathrm{Act}} + K_{\mathrm{Act}}} \frac{C_{\mathrm{But}}}{C_{\mathrm{But}} + K_{\mathrm{But}}} \frac{C_{H_2}}{C_{H_2} + K_{H_2}}. \tag{7}$$

Here, the maximum rates of acetogenesis, butyrate and caproate elongation are denoted by $q^{max}_{Act^-}$, q^{max}_{But}, q^{max}_{Cap} (mol m^{-2} s^{-1}), with the corresponding actual rates denoted by q_{Act^-}, q_{But}, q_{Cap}, respectively, and the parameters are listed in **Supplementary information S11**.

2.2. Electrochemical reactions

For the above biochemical reactions (Eqs. (1)–(3)) to occur, electrons need to be transferred from the cathode to the microbial redox centers (cytochromes). In this system, electrochemically produced H_2 mediates electrons to the microbes. In general, electrochemical evolution of H_2 occurs in acidic solution by reducing protons (Eq. (8)) and in alkaline solution by reducing water (Eq. (9)) [38]. The pH of the catholyte is slightly acidic (nearly neutral), and hence, HER can occur from both H^+ and H_2O.

$$H^+ + e^- \longrightarrow \frac{1}{2}H_2 \quad \Phi_o = 0\,\text{V [vs] SHE} \tag{8}$$

$$H_2O + e^- \longrightarrow \frac{1}{2}H_2 + OH^- \quad \Phi_o = 0\,\text{V [vs] SHE} \tag{9}$$

Here Φ_o is the equilibrium potential at pH = 0 [39,40]. Several studies have indicated that the proton-based hydrogen evolution dominates at low cathodic overpotential, and as the cathodic overpotential increases, a rapid consumption of protons occurs near the electrode, creating a pH difference between the bulk and the electrode (in case of an unbuffered or not well-buffered system). Consequently, the HER from H^+ becomes transport-limited, and HER from H_2O dominates [41–47]. The Butler–Volmer current density from both these cathodic half-reactions is given by:

$$j_{H^+} = -j_o^{H^+}\left[\left(\frac{C_H^+}{C_{H^+}^{ref}}\right)\exp\left(\frac{-\alpha_{H^+}F\eta_c}{RT}\right)\right], \tag{10}$$

$$j_{H_2O} = -j_o^{H_2O}\left[\exp\left(\frac{-\alpha_{H_2O}F\eta_c}{RT}\right)\right], \tag{11}$$

where j_o is the exchange current density (A m^{-2}) for a graphite electrode and $C^{ref}_{H^+}$ is the reference proton concentration in mol m^{-3} (**Supplementary information S2**). The overpotential with pH correction is defined as $\eta_c = (\Phi_s - \Phi_l) - \left(\Phi_o - \frac{2.303RT}{F}\text{pH}\right)$ in V, which is valid when pH+pOH=14. Here, Φ_s is the cathode potential (vs SHE) at the biofilm-electrode interface and Φ_l is the electrolytic potential at the cathode interface.

2.3. Homogeneous reactions

Concurrent with the heterogeneous biochemical and electrochemical reactions, the electrolyte undergoes homogeneous volumetric reactions. Autoprotolysis of water (Eq. (12)) is possible due to the presence of protons (transported from the anodic chamber, produced from buffer) and hydroxide ions (produced as a byproduct of HER from water) [48]. The phosphate compounds are the main buffers in the system, assigned to regulate the pH [49]. For simplicity, only the dissociation of dihydrogen phosphate in Eq. (13) ($H_2PO_4^-$, pKa = 7.21) is considered, as it is relevant to the operating pH, while the further dissociation of hydrogen phosphate (HPO_4^{2-}, pKa = 12) is neglected. The system can also produce bicarbonate (HCO_3^-) through CO_2 hydrolysis (Eq. (14)). Further dissociation to CO_3^{2-} is not considered (**Supplementary information S13** shows its minor influence).

$$\begin{aligned} &H_2O \underset{}{\overset{k^f_{H_2O}}{\rightleftharpoons}} H^+ + OH^-, \\ &r_{H_2O} = k^f_{H_2O}\left(1 - \frac{C_{OH^-}C_{H^+}}{\mathcal{K}^{eq}_{H_2O}}\right) \end{aligned} \tag{12}$$

$$\begin{aligned} &H_2PO_4^- \underset{k^f_{H_2PO_4^-}}{\overset{k^f_{H_2PO_4^-}}{\rightleftharpoons}} HPO_4^{2-} + H^+, \\ &r_{H_2PO_4^-} = k^f_{H_2PO_4^-}\left(C_{H_2PO_4^-} - \frac{C_{HPO_4^{2-}}C_{H^+}}{\mathcal{K}^{eq}_{H_2PO_4^-}}\right) \end{aligned} \tag{13}$$

$$\begin{aligned} &CO_2 + H_2O \underset{k^f_{CO_2}}{\overset{k^f_{CO_2}}{\rightleftharpoons}} H^+ + HCO_3^-, \\ &r_{CO_2} = k^f_{CO_2}\left(C_{CO_2} - \frac{C_{HCO_3^-}C_{H^+}}{\mathcal{K}^{eq}_{CO_2}}\right) \end{aligned} \tag{14}$$

The rate (r_i [mol m^{-3} s^{-1}]) and direction of each reaction are be determined from the local concentration of the reactants and products, the forward rate (k_i^f) and equilibrium constants ($\mathcal{K}_i^{eq}$). These reactions are much faster than the electro- and biochemical reactions, and the values of the parameters used for these homogeneous reactions are listed in **Supplementary information S11**. The bulk region of the domain is assumed to be in chemical equilibrium, and the estimations are in **Supplementary information S5**.

2.4. Diffusion boundary layer

The diffusion boundary layer in the vicinity of the biofilm creates an external mass transfer resistance, which can result in a difference in concentration between the biofilm surface and the bulk region. The bulk velocity can also affect the thickness of the concentration boundary layer, and hence it is essential to include their effect while estimating the mass transfer coefficient for each species entering or exiting the domain [17,50–53]. Under continuous operation with average bulk flow velocity, the Sherwood number (Sh) correlation is used to estimate the altered mass transfer coefficient $\left(\beta_i = \text{Sh}_i(D_i/d_h)\right)$. The Sherwood number of a species (i), related to the Schmidt number (Sc), Reynolds number (Re), and hydraulic diameter of the flow channel(d_h), is given by [17]:

$$\text{Sh}_i = 2\text{Re}^{0.5}\text{Sc}_i^{0.5}\left(d_h/L_c\right)^{0.5}(1 + 0.0021\text{Re}) \tag{15}$$

$$\text{Re} = \frac{ud_h}{\nu}, \quad \text{Sc}_i = \frac{\nu}{D_i} \tag{16}$$

2.5. Mass and charge balance

The species transport in an electrolyte is generally driven by diffusion, migration, and convection. By comparing the transport scaling for migration velocity and flow velocity across the biofilm with the species diffusion, the flow-based Peclet number was found to be negligible ($\text{Pe}_{\text{flow}} \ll 1$) (**Supplementary information S1**). The Nernst–Planck equation with the volumetric source term ($\sum R_i$ in mol m^{-3} s^{-1}) governs the species transportation and mass conservation (Eq. (17)). For any soluble component i, the mass conservation is set up by diffusion ($\mathbf{N}_i^{\text{Diff}} = -D_i\nabla C_i$) and migration transport ($\mathbf{N}_i^{\text{Mig}} = -\frac{Z_iD_iC_iF\nabla\Phi_l}{RT}$) excluding convection ($\mathbf{N}_i = \mathbf{N}_i^{\text{Diff}} + \mathbf{N}_i^{\text{Mig}}$). The steady-state form of Eq. (17) is solved in the electrolyte region.

$$\frac{\partial C_i}{\partial t} = -\nabla\cdot\left(-D_i\nabla C_i - \frac{Z_iD_iC_iF\nabla\Phi_l}{RT}\right) + \sum R_i \tag{17}$$

The species diffusion coefficients D_i (m^2 s^{-1}) correspond to the bulk values and Z_i denotes the species valency. Because the electric double layer is negligibly thin at the microbe scale, local electroneutrality is assumed. Consequently, current conservation ($\nabla\cdot\boldsymbol{i} = 0$ elaborated in Eq. (18) together with the electroneutrality condition ($\sum_i Z_iC_i = 0$) are used to estimate the electrolyte potential gradient ($\nabla\Phi_l$), which drives

ion migration. The local ionic conductivity k (S m^{-1}) in Eq. (18) is given in Eq. (19).

$$\nabla \cdot \left((k + k')\nabla \Phi_l\right) + F\nabla \cdot \left(\sum_i Z_i D_i \nabla C_i\right) = 0 \tag{18}$$

$$k = \frac{F^2}{RT} \sum_i \left(Z_i^2 D_i C_i\right). \tag{19}$$

In Eq. (18), the ionic conductivity is decomposed into the contribution from the reacting (k) and non-reacting (k') ions in the catholyte. The drift flux contribution towards ionic current from the non-reacting metabolites is neglected, and a uniform ionic conductivity (k') is estimated using their corresponding bulk concentrations. This provides computational ease by only solving for the species involved in chemical reaction, i.e., i = CO_2, H_2, H^+, Act^-, But^-, Cap^-, HCO_3^-, $H_2PO_4^-$, HPO_4^{2-}, OH^-. The electrochemical and biochemical reaction rates are modeled as fluxes of respective species, while the homogeneous reaction rates are modeled as volumetric sources. At the electrode–electrolyte interface (Γ_e), the boundary conditions for Eq. (17) and (18) are net flux and current density, respectively, as shown in Eq. (20), which is based on Butler–Volmer kinetics.

$$\begin{cases} \boldsymbol{N}_i \cdot \vec{n} = -\dfrac{\nu_{i,H^+} j_{H^+} + \nu_{i,H_2O} j_{H_2O}}{F} \\ \boldsymbol{i} \cdot \vec{n} \quad = j \end{cases} \quad \text{on } \Gamma_e \tag{20}$$

The stoichiometric coefficients of species in HER from H^+ and H_2O are represented as ν_{i,H^+} and ν_{i,H_2O}, respectively. Their respective current density and number of electrons in each reaction are j_{H^+} and j_{H_2O}, and n_{e,H^+} and n_{e,H_2O}. For the species not involved in the HER, the net flux will be zero at that interface (Γ_e). On the microbe-electrolyte interface (Γ_b), the Michaelis–Menten reaction rates are modeled as fluxes and the current density is computed using the sum of all the source/sink fluxes at the interface, as shown in Eq. (21). The exit boundary (Γ_d) is assumed to be in the diffusion boundary layer. Since the flux across the diffusion boundary layer is theoretically constant, the mass transfer type boundary condition in Eq. (22) can be used at any distance within the diffusion boundary layer. A zero electrolyte potential is set at the exit boundary for the current conservation equation.

$$\begin{cases} \boldsymbol{N}_i \cdot \boldsymbol{n} = Q_i \\ \boldsymbol{i} \cdot \boldsymbol{n} \quad = F \sum_i Z_i Q_i \end{cases} \quad \text{on } \Gamma_b \tag{21}$$

$$\begin{cases} \boldsymbol{N}_i \cdot \boldsymbol{n} = \beta_i (C_i - C_{i,\infty}) \\ \Phi_l \quad = 0 \end{cases} \quad \text{on } \Gamma_d \tag{22}$$

The values of the physical and biochemical parameters employed in the model are summarized **Supplementary information S11**.

3. Results and discussion

First, the model is validated by comparing the effective ionic conductivity against the Bruggeman correlation, and for reactions, the product ratio was compared with experimental results for corresponding current densities. The transport model used in this work is validated by simulating a non-reactive system with poly-dispersed spheres and comparing the effective ionic conductivity from simulations with the Bruggeman correlation. The system description and results, such as local potential gradient and species fluxes, are given in the **supplementary information S4**. The Bruggeman correlation is widely used to quantify effective transport properties for porous media, but the expression is strictly suitable only for a packing of poly-dispersed spheres. Fig. 2 shows that the effective conductivity from simulation agrees well with the Bruggeman correlations. We also note that the effective conductivity of the biofilm, which we model as a layer of densely-packed spherocylindrical microbes, is higher than that of a poly-disperse sphere packing of the same volume fraction (red markers in Fig. 2) and should thus not be estimated with a Bruggeman correlation. The relative effective conductivity (k_{eff}/k_o) of the biofilm is ≈ 41%, consistent with other numerical works [54,55].

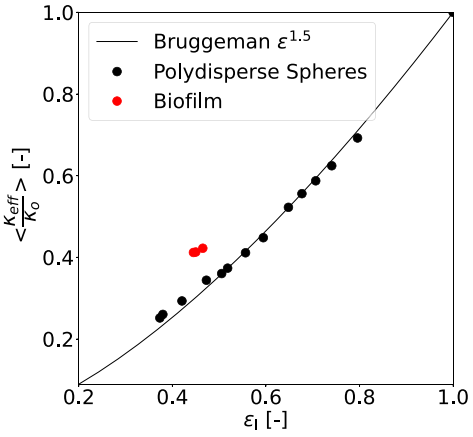

Fig. 2. Relative effective ionic conductivity against porosity.

Next, a preliminary check on the microbial bio-kinetics is performed by comparing the product ratios towards the desired products (Eq. (23)) to those reported experimentally by Jourdin et al. [23]. The reported current densities in the experiments are scaled to the projected area rather than the actual electrode area within the 3D carbon felt. This scaled current density is relevant for our comparison because the external biofilm is considered in this study.

$$\mathcal{R}_i = \frac{n_i \mathcal{P}_i}{\sum_i n_i \mathcal{P}_i}, i = Act^-, But^-, Cap^-. \tag{23}$$

Here, n_i and $\mathcal{P}_i$ represent the number of carbon atoms and the production rates of the carboxylic acids, respectively. Fig. 3 shows that the ratio of carboxylic acid products from our simulation agrees well with the experiments, especially for the thicker biofilms considered in this study. However, we note that the biofilm thickness in the experiments is not controllable and can vary in space and time. Therefore, it is important to gain insight into how the bioelectrochemical process depends on the biofilm thickness, rather than only modeling the single biofilm that agrees best with the global experimental outcomes.

3.1. Performance parameters: carbon selectivity

In the following, the validated model is used to investigate macroscopic parameters such as carbon selectivity towards different products, the H_2 transfer efficiency, and CO_2 uptake efficiency under the effect of cathode potential (Φ_s) and the BFT. First, we evaluate the carbon selectivity towards the various products, defined as:

$$S_i = \left|\frac{n_i \mathcal{J}_i}{\mathcal{J}_{CO_2}}\right|_{\Gamma_o} = \left|\frac{n_i \iint_{\Gamma_o} \mathbf{N}_i \cdot \vec{n}\, d\Gamma_o}{\iint_{\Gamma_o} \mathbf{N}_{CO_2} \cdot \vec{n}\, d\Gamma_o}\right|, \quad i = Act^-, But^-, Cap^-, HCO_3^- \tag{24}$$

where n_i and $\mathcal{J}_i$ (in mol s^{-1}) denote the number of carbon atoms and the net rate of the ith species entering or exiting the domain, respectively. At steady state, the production or consumption rates can be related to the species flux exiting/entering the domain, respectively. Before using Eq. (24), the carbon conservation in the domain was verified (**supplementary information S7**). Fig. 4 shows that the acetate selectivity (S_{Act^-}) decreases as the biofilm thickness increases, in favor of the butyrate and caproate selectivity. In Fig. 4a, the thinner biofilms (30, 60 μm) show a peak in S_{Act^-} for Φ_s = −0.95 V and −1.05V, respectively. With the increase in cathode potential (Φ_s), the selectivity increases

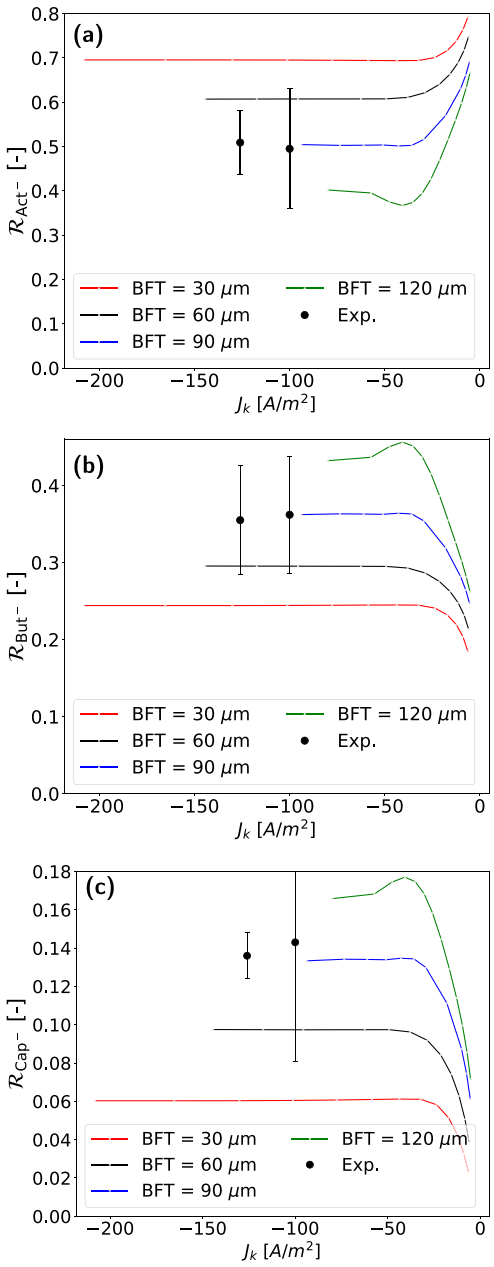

Fig. 3. Preliminary comparison between simulated and experimental [23] product ratios of **(a)** acetate, **(b)** butyrate, and **(c)** caproate.

until it peaks due to the enhanced biochemical conversion limited by the H_2 production at the electrode. On further increasing the magnitude of Φ_s, the acetate selectivity (S_{Act^-}) decreases due to two factors, namely (i) the CO_2 consumption for biochemical conversion becomes insensitive to an increase in electrode potential (Φ_s), as can be inferred from Fig. 5a. (ii) Moreover, the increasing magnitude of the cathodic potential (Φ_s) causes an increase in the pH across the biofilm (Fig. 5b) due to the increased electrochemical OH^- production. This drives consumption of CO_2 through homogeneous carbonation (4d), leaving less CO_2 available for biochemical conversion to acetate (Act^-). For HCO_3^-, the suppression of biochemical activity by H_2 at low $|\Phi_s|$ leads to a greater proportion of CO_2 being diverted toward CO_2 hydrolysis (Eq. (14)).

The caproate selectivity (S_{Cap^-}) is the lowest of the products due to the low reaction rate of biochemical elongation to caproate and the intermediates are transported out of the biofilm faster due to their higher diffusion coefficient ($D_{Act^-} > D_{But^-} > D_{Cap^-}$). In Figs. 4b and 4c, the thicker biofilms are more selective towards butyrate and caproate, with S_{Cap^-} reaching a maximum of ≈0.14 for BFT = 120 μm. The residence time of the intermediate species namely, acetate $\left(L_b^2/D_{eff,Act^-}\right)$ and butyrate $\left(L_b^2/D_{eff,But^-}\right)$ increases for thicker biofilms, favoring biochemical elongation to butyrate and caproate. The dimensionless Damköhler number ($Da_i = \tau_{reaction}/\tau_{transport}$), which represents the ratio of the reaction time to the transport time, can be used to explain the effect of BFT on biochemical elongation. In case of acetate, $Da_{Act^-} \approx 1.25$ for BFT = 30 μm, whereas $Da_{Act^-} \approx 0.33$ for BFT = 120 μm. This indicates that the thicker biofilms have a longer timescale for transport, facilitating better utilization of intermediates for biochemical elongation.

3.2. *Performance parameter:* H_2 *transfer and* CO_2 *consumption efficiency*

The H_2 produced at the electrode–electrolyte interface is utilized by the microbes as it diffuses across the biofilm. The evolved H_2 might not be completely utilized for biochemical CO_2 reduction [24] and ultimately exit the biofilm, lowering the current efficiency and energy-input efficiency of the process. If the consumption rate of H_2 is lower than its production rate, the excess H_2 will exit the domain to the bulk. Hence, we define a hydrogen transfer efficiency (η_{H_2}) to characterize the system performance as the ratio of the hydrogen consumed by the biocatalyst (Γ_b) to the hydrogen produced electrochemically at the cathode (Γ_e):

$$\eta_{H_2} = \frac{\iint_{\Gamma_b} \mathbf{N}_{H_2} \cdot \vec{n} \mathrm{d}\Gamma_b}{\iint_{\Gamma_e} \mathbf{N}_{H_2} \cdot \vec{n} \mathrm{d}\Gamma_e} \times 100. \tag{25}$$

In Fig. 6a (black lines), for lower magnitude cathodic potential ($|\Phi_s|$), η_{H_2} is 100% due to low electrochemical production of H_2. The threshold $|\Phi_s|$ at which η_{H_2} deviates from 100% increases with increasing biofilm thickness, i.e. above $\Phi_s \approx -0.9$ V, η_{H_2} deviates from 100% for BFT = 30 μm, while the deviation from maximum η_{H_2} in BFT = 120 μm is from $\Phi_s \approx -1.2$ V . This is mainly due to the increased demand for hydrogen by the biocatalyst over a longer distance from the electrode in thicker biofilms. In addition, the 2 other factors contributing to the drop in performance in thicker biofilms are (i) the ohmic potential drop is higher for thicker biofilms (see **Supplementary information S9**), resulting in a reduction of overpotential magnitude for the electrochemical reaction and, (ii) the pH at the cathode–electrolyte interface (Fig. 5b) increases with biofilm thickness, resulting in a higher magnitude of the equilibrium potential for hydrogen evolution reaction due to the Nernst potential shift. From Fig. 6a, though η_{H_2} remains 100% even at lower $|\Phi_s|$, this comes at the cost of the CO_2 consumption efficiency (η_{CO_2}), which we define as:

$$\eta_{CO_2} = \frac{1}{q^{max}_{Act^-}} \left(\frac{\iint_{\Gamma_b} Q_{CO_2} \mathrm{d}\Gamma_b}{\iint_{\Gamma_b} \mathrm{d}\Gamma_b} \right) \times 100. \tag{26}$$

For low $|\Phi_s|$, the 100% hydrogen transfer efficiency combined with a low CO_2 consumption efficiency indicates that the CO_2 conversion rate is limited by a lack of available H_2. As $|\Phi_s|$ increases, a maximum CO_2 consumption efficiency of ≈ 60% is measured for the 30 μm thick biofilm and the efficiency decreases for thicker biofilm ($\eta_{CO_2} \approx 40\%$ for BFT =120 μm). This effect is due to the increase in the diffusive mass transfer barrier for CO_2 from the bulk, resulting in a reduced concentration of CO_2 for conversion by the microbes. These results emphasize a key trade-off: while thicker biofilms are favorable for H_2 retention, thinner biofilms support better CO_2 utilization, underscoring the importance of optimizing both biofilm thickness and cathode potential for enhanced performance in bio-electrochemical systems. The overall efficiency ($\eta_o = \eta_{H_2} \times \eta_{CO_2}$) for H_2 and CO_2 usage as a function

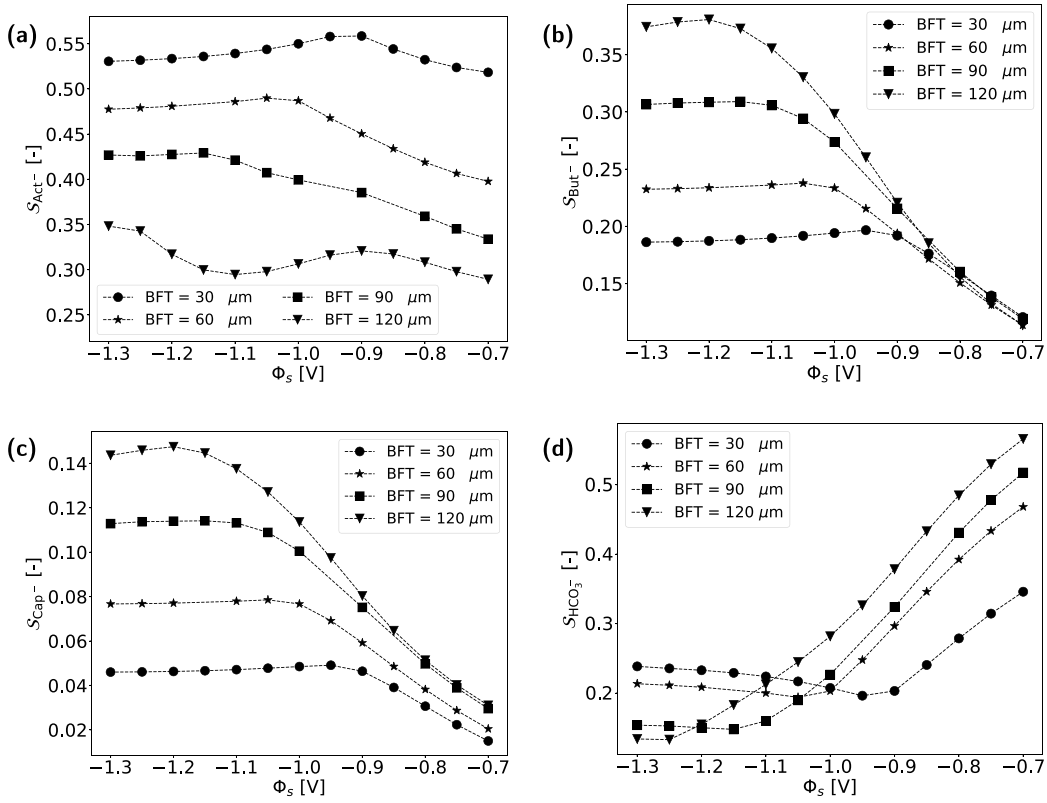

Fig. 4. Carbon selectivity towards **(a)** Act^-, **(b)** But^-, **(c)** Cap^-, **(d)** HCO_3^- as a function of Φ_s and BFT for $C_{CO_2,\infty} = 10$ mM.

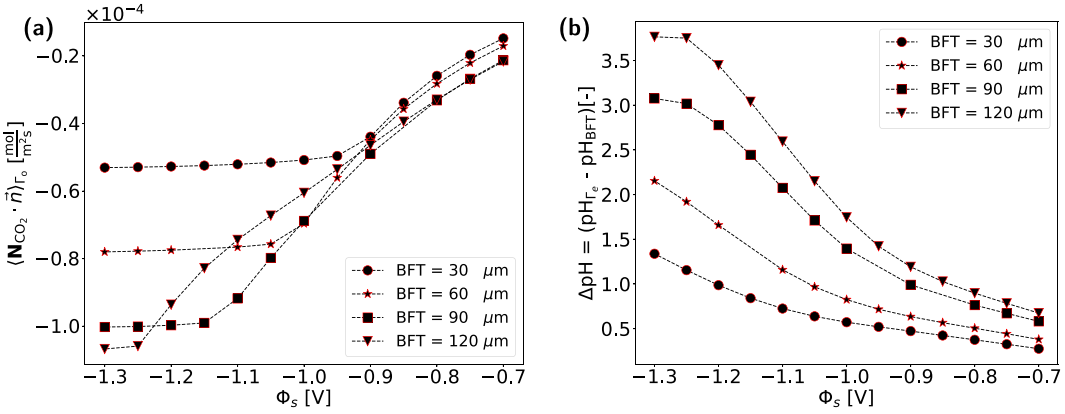

Fig. 5. **(a)** CO_2 flux at the exit boundary and **(b)** pH difference across the biofilm.

of Φ_s and BFT are shown in Fig. 6b. The results indicate that there is an optimal electrode potential (Φ_s) for a corresponding BFT at which the overall efficiency is maximum. To the right of this peak (towards lower magnitude cathodic potential), η_o decreases due to an inefficient CO_2 conversion rate, owing to the lack of sufficient H_2 produced at the electrode. On the other hand, the decrease in η_o to the left of this peak is caused by the decreasing hydrogen transfer efficiency, due to excess electrochemical H_2 production. Thinner biofilms (30–60 μm) achieve higher peak efficiencies, with the maximum observed at ≈60% for 30 μm at Φ_s ≈−1.0 V. In contrast, increasing the BFT to 120 μm yields a marked reduction in efficiency (≈40%). Overall, the thicker biofilm favors higher S_{Cap^-} and enhanced H_2 retention, but the CO_2 consumption efficiency is reduced and vice versa for thin biofilms.

3.3. Local field variables: gradients

Micro-scale parameters such as the concentration gradient, local pH, biochemical rates, and electrolyte potential (Φ_l) within the biofilm are crucial, as they provide mechanistic insight into the macroscopic behavior observed earlier. Fig. 7a shows a decrease in CO_2 concentration from the biofilm surface towards the electrode, reflecting microbial consumption, while Fig. 7b highlights the heterogeneous CO_2 flux distribution with local maxima in the vicinity of the biofilm. A 3D resolved model is essential to resolve such spatial heterogeneity and identify localized activity, which can then be condensed into 1D profiles by averaging over the electrolyte in cross-sectional planes parallel to the electrode surface. In the following, we will compare such 1D profiles for different Φ_S.

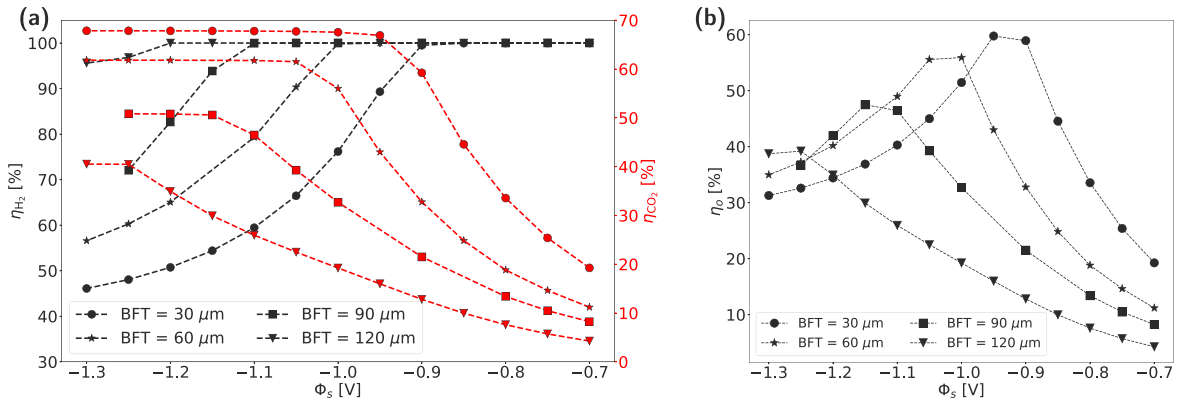

Fig. 6. **(a)** Hydrogen transfer (η_{H_2}) (black lines) and CO_2 consumption efficiency (η_{CO_2}) (red lines), **(b)** Overall efficiency (η_o) as a function of Φ_s and BFT for $C_{CO_2,\infty}$ = 10 mM.

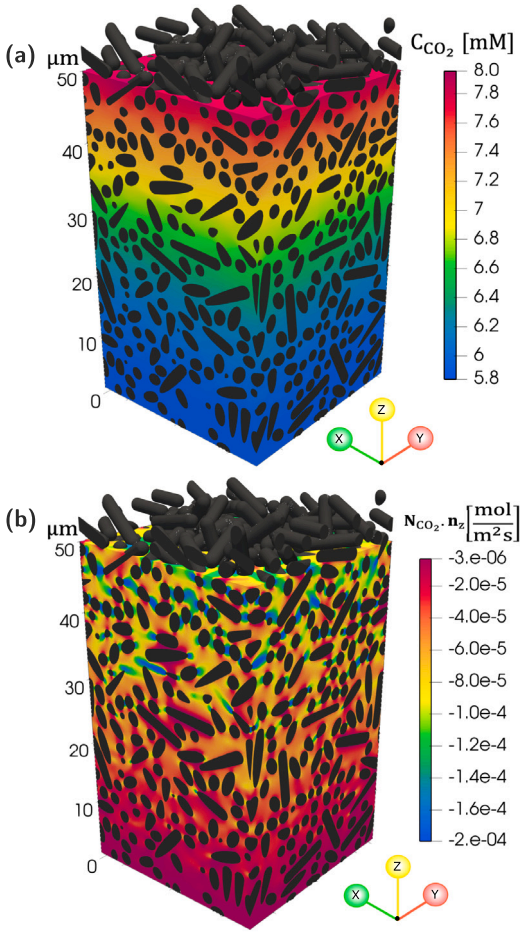

Fig. 7. **(a)** Local concentration and **(b)** net flux of CO_2 across the biofilm for BFT = 60 μm at Φ_s = −1.0 V.

The concentration gradient and local biochemical conversion rates are discussed for the thin and thick biofilm, i.e., BFT = 30 and 120 μm (results for other BFTs in **Supplementary information S9**). Fig. 8 shows the concentration and the biochemical reaction rate as a function of the distance from the electrode for the 30 μm thick biofilm. From Fig. 8a, the local CO_2 concentration (black lines) across the biofilm decreases as the cathodic potential is increased, which is due to the increased CO_2 consumption rate (q_{CO_2}) (red lines). It is due to the high production of H_2 at the electrode interface (from Fig. 8b) that improves the CO_2 consumption across the biofilm. Although the H_2 production increases (resulting in higher concentration across the biofilm) by increasing the cathodic potential from Φ_s = −1.1 V to Φ_s = −1.3 V, there is no significant change in the local CO_2 concentration. Conversely, the local concentration of H_2 across the biofilm is significantly higher compared to its half-saturation constant ($C_{H_2} \gg k_{H_2}$) for cathodic potential greater than −1.1 V, resulting in the acetogenesis rate not being affected by local H_2 concentration, as can be seen from $\mathcal{Q}_{CO_2}$ in 8a. Fig. 8b shows that, although the H_2 concentration increases with $|\Phi_s|$, its biochemical consumption rate remains unchanged for Φ_s < −1.1 V, inferring that the excess H_2 diffuses into the bulk, consistent with the observed trend in hydrogen transfer efficiency in Fig. 6a. As H_2 drives acetogenesis and chain elongation to butyrate and caproate, regions of the biofilm deprived of cathodically produced H_2 remain inactive.

At low $|\Phi_s|$, H_2 production is insufficient to meet biocatalyst demand, creating inactive biofilm zones with negligible conversion rates (red-solid lines in Fig. 8). The inactive zone decreases with increasing $|\Phi_s|$, and above 1.0 V, the local biochemical conversion rates do not change with increasing $|\Phi_s|$. From Fig. 8a, when H_2 no longer limits the reaction rates, maximum acetogenesis occurs at the biofilm outer surface, where CO_2 concentration is highest. Thus, at $|\Phi_s|$ greater than this threshold, CO_2 transport rather than H_2 availability limits acetogenesis. At high cathodic potential ($|\Phi_s|$ > 1.0 V), the local production rates of acetate and caproate are not highly influenced by the cathode potential. The local net production rate of acetate (q_{Act^-}) has a marginal increase from cathodic potential of −1.0 V to −1.3 V, but there is a decrease in its local concentration. This is because the increase in cathodic potential results in an increase in the magnitude of the electric field and the migrating flux of the ionic species. Hence, there is an increase in the acetate migrating out of the biofilm with an increase in cathodic potential, while the acetogenesis rate remains unchanged. The consequence of this effect is a marginal reduction in the local production rates of caproate (q_{Cap^-}), due to the reduced acetate concentration available for the chain elongation process to butyrate and caproate. This can be seen from Fig. 8d, where there is a reduction in concentration and production rate of caproate.

For the 120 μm biofilm, the interplay of migration, electrochemical, and biochemical reactions leads to dominant mass transfer limitations. The greater thickness increases transport resistance, producing larger concentration gradients than in the 30 μm case. Fig. 9 shows the corresponding concentrations and biochemical fluxes of reactants and products. From Fig. 9b, the cathodic potential at which the H_2 is available throughout the 120 μm thick biofilm is greater than that for the system with 30 μm BFT. In terms of acetogenesis from Figs. 9a, 9b, 9c, the reduction in magnitude of biochemical flux of CO_2, H_2, and acetate is significant in the deeper region of the biofilm (region close to the electrode) at higher $|\Phi_s|$. For a lower $|\Phi_s|$, the maximum

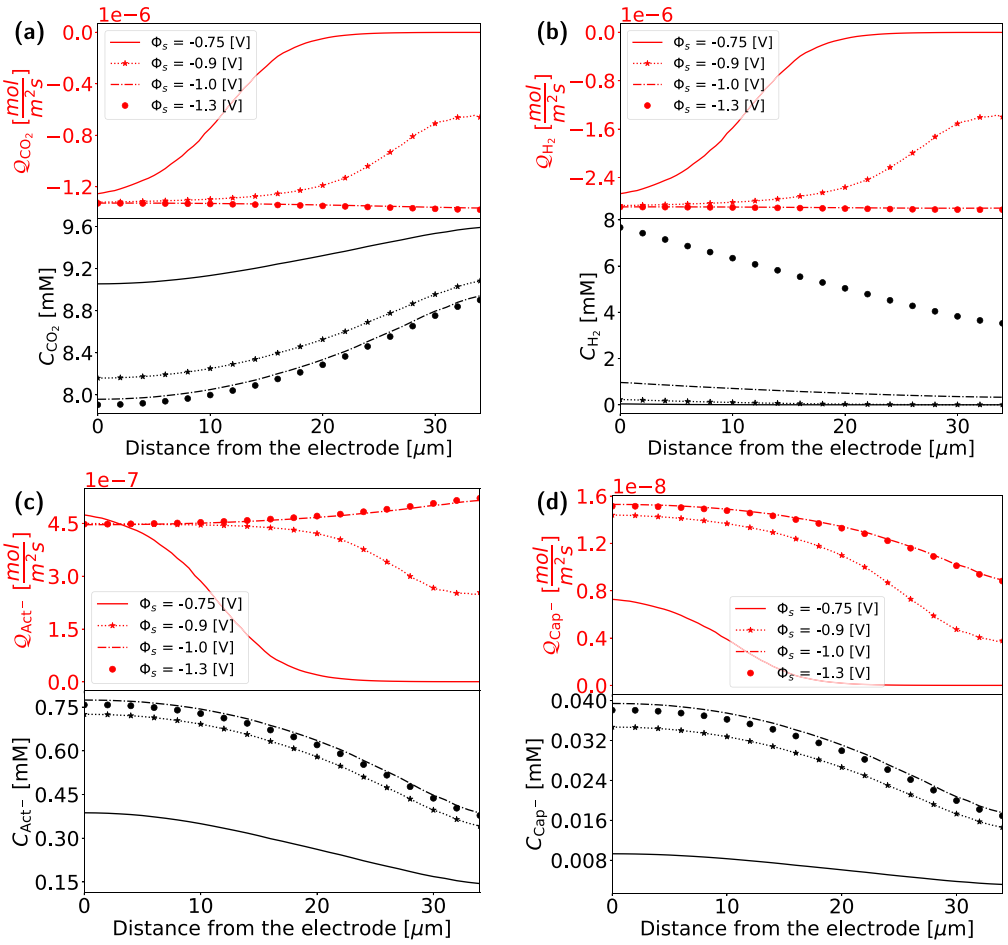

Fig. 8. Concentration and biochemical flux profiles of **(a)** CO_2 **(b)** H_2 **(c)** Act^- **(d)** Cap^- across 30 μm biofilm at Φ_s = [−0.75, −0.9, −1.0, −1.3]V.

biochemical flux for acetogenesis is near the electrode. This behavior reflects the confinement of hydrogen to the immediate electrode vicinity, where its concentration is sufficient to sustain biochemical activity, while the remainder of the biofilm experiences negligible flux. On further increasing the cathodic potential, from −0.75 V to −0.9 V, there is a reduction in the maximum value of biochemical flux. This is because the increased hydrogen production results in a wider active region across the biofilm, which acts as a CO_2 sink. The consumption of CO_2 by the biocatalyst at the far end of the active region results in a decreased concentration of CO_2 very close to the electrode. This causes a reduction in the acetogenesis reaction rate due to the concentration of CO_2 approximately equal to its half-saturation constant ($C_{CO_2} \approx k_{CO_2}$) near the electrode (as a result of it diffusing over a thicker biofilm). The acetogenesis reaction rate is faster than the chain-elongation reaction rates and hence the local reaction rates of acetate, H_2, and CO_2 are mainly influenced by q_{Act^-}. Although there is a decrease in the magnitude of q_{Act^-} across the active zone while shifting from Φ_s = −0.75 V to −0.9 V, the production rate q_{Cap^-} increases in magnitude. The acetate concentration close to the electrode increases with increasing Φ_s from −0.75 V to −0.9 V, and it is the reactant for the production of both butyrate and caproate along with H_2, which is available near the electrode.

On further increasing the absolute value of cathodic potential (to Φ_S = −1.1 V), the peak in $\mathcal{Q}_{Act^-}$ shifts away from the electrode within the active region of the biofilm, due to the relatively high amount of CO_2 and H_2 available away from the electrode. Also, the net biochemical flux of acetate ($\mathcal{Q}_{Act^-}$) near the electrode is significantly below the maximum value at a distance of approximately 75 μm from the electrode. The aforementioned reason is that the increased availability of CO_2 away from the electrode results in an increase in the magnitude of the sink term (q_{CO_2}), thereby lowering the CO_2 concentration near the electrode, as shown in Fig. 9a. This results in lower production of acetate near the electrode and hence lowering S_{Act^-} in Fig. 4a. At Φ_s = −1.3 V, the H_2 production rate at the electrode–electrolyte interface surpasses its demand at the bio-electrolyte interface, as can also be inferred from the η_{H_2} in Fig. 6a. In such a case, similar to the 30 μm thick biofilm, the maximum production rate of acetate shifts towards the outer part of the biofilm, but there is a significant decrease in the $\mathcal{Q}_{Act^-}$ near the electrode. In fact, from Fig. 9c (Φ_s = −1.3 V), there is a net consumption of acetate near the electrode surface ($\mathcal{Q}_{Act^-} < 0$), indicating that the acetogenesis rate is slower than the net rate of the chain-elongation reactions (to butyrate and caproate using acetate). The expanding active zone with increasing $|\Phi_s|$ results in a decrease in the CO_2 concentration ($C_{CO_2} < k_{CO_2}$) near the electrode due to diffusion limitations. The acetate produced at the outer end of the biofilm (maximum local $\mathcal{Q}_{Act^-}$) exits immediately to the bulk, resulting in an increase in selectivity towards acetate again in Fig. 4b. Eventually, the caproate production rate is lower at the outer end of the biofilm due to the fast transport of intermediates, i.e., acetate and butyrate. Thus, the interplay between H_2 availability, CO_2 transport, and intermediate migration observed from the microscale results rationalizes the efficiency trends and selectivity shifts, confirming that spatial heterogeneity within the biofilm governs both global consumption efficiency and the product spectrum.

Although this model addresses the critical performance parameters and the transport limitations at the microbe scale, several limitations must be pointed out. Firstly, although the simulated current densities agree reasonably with preliminary experimental data, the

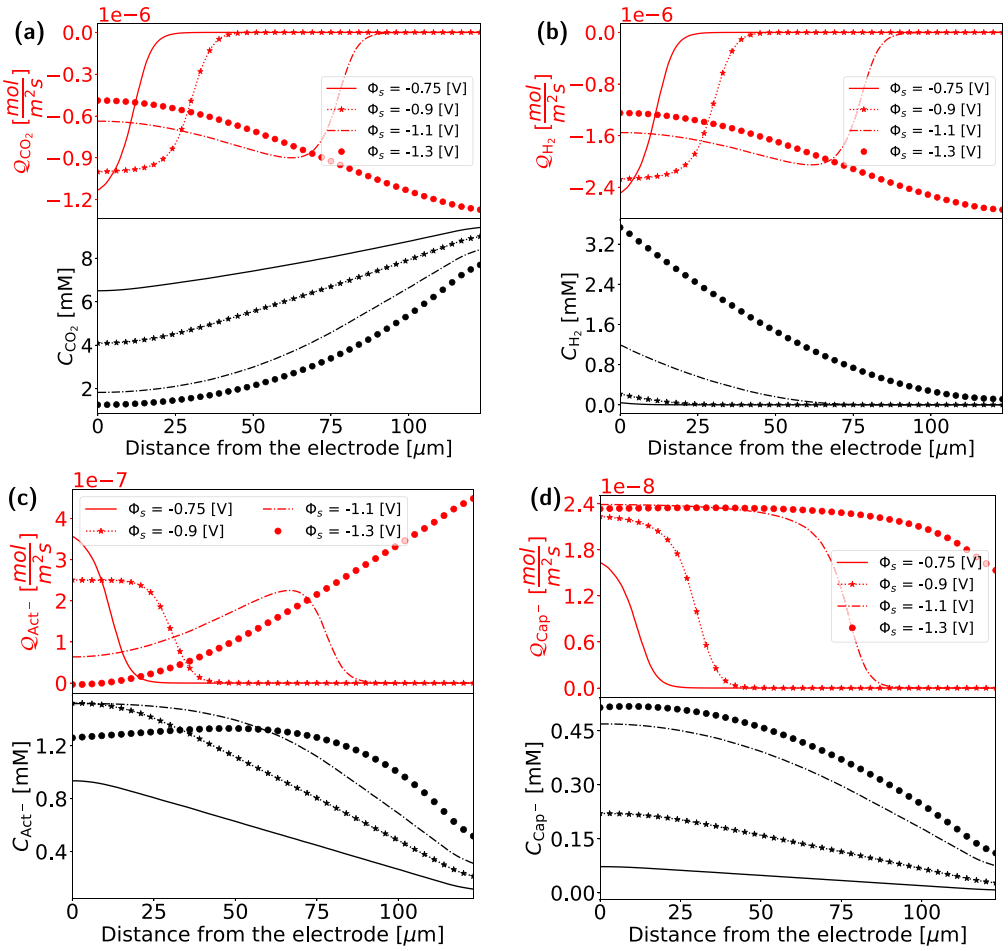

Fig. 9. Concentration and biochemical flux profiles of **(a)** CO_2 **(b)** H_2 **(c)** Act^- **(d)** Cap^- across 120 μm biofilm at Φ_s = [−0.75,−0.9,−1.1,−1.3] V.

literature-derived kinetic parameters do not fully capture graphite felt characteristics under relevant conditions: the precise relation between current density and applied potential will depend on particulars of the electrode (graphite felt) material. The model considers that all the microbes within the biofilm can perform acetogenesis and the chain elongation process. In reality, the microbe strain responsible for chain elongation can be different from the acetogens. In such a case, an altered thermodynamic approach with additional Gibbs energy for anabolism (ΔG_{An}^{Act}, ΔG_{An}^{But}, ΔG_{An}^{Cap}) must be considered, which can alter the overall stoichiometry of the metabolites due to different catabolic factors [16]. The local biochemical activity, which is affected by the pH (pH inhibition), is not considered in the model. On knowing the optimal pH for each biochemical process, the Michaelis–Menten equation can be corrected for local pH [20,56]. This multi-chemical species single-phase model does not account for H_2 bubble nucleation at the electrode when the local solubility limit is exceeded. These detached bubbles can affect the biofilm structure, which is not included in this model. Finally, the biofilm model considered in this work is a small fraction of a bigger reactor-scale system, indicating that cell-scale simulation will allow for a more direct comparison with experiments. Further, microelectrode-based experimental information on the local gradients of CO_2 and pH can aid in better validation of such micro-scale models.

4. Conclusion

In this work, we have developed a three-dimensional resolved model of the biofilm in a microbial electrosynthesis cell. The model describes species transport across the biofilm involved in electrochemical, biochemical, and acid–base reactions. We have studied the case of a cathodic biofilm that can fix CO_2 into acetate and further to butyrate and caproate using H_2 as the charge-transfer mediator (MET).

Our results show that CO_2 utilization, H_2 transfer efficiency, and product selectivity are strongly influenced by both the applied electrode potential and the biofilm thickness, with the optimum performance arising from a balance between these two factors. For each biofilm thickness, there exists a threshold cathode potential below which the local concentration and biochemical activity are limited by the local H_2 concentration. Beyond this threshold of $|\Phi_s|$, the local gradients are limited by the transport of CO_2 and intermediates like acetate and butyrate (sensitive to biofilm thickness). Thicker biofilms enhance chain elongation to butyrate and caproate, while thinner biofilms favor an efficient CO_2 conversion. Thus, this work reveals the transport and reaction limitations that govern system performance, providing a mechanistic basis for optimizing operating conditions. These findings can be extended to formulate strategies for selective inoculation of microbes in a multi-culture biofilm, if the microbe strain is known for each biochemical reaction.

CRediT authorship contribution statement

V. Murugesan: Writing – original draft, Visualization, Methodology, Investigation, Conceptualization. **Remco Hartkamp:** Writing – review & editing, Visualization, Supervision, Investigation, Formal analysis. **Johan T. Padding:** Writing – review & editing, Visualization, Supervision, Investigation, Funding acquisition, Formal analysis.

Declaration of competing interest

The authors declare that they have no known competing financial interests or personal relationships that could have appeared to influence the work reported in this paper.

Acknowledgments

This project received funding from the project "C1to6: CO_2 into hexanoic acid using microbial electrosynthesis" (NWO OTP 19771). We thank **Dr. Ludovic Jourdin** for his tips and advice and for providing experimental insights.

Appendix A. Supplementary data

Supplementary material related to this article can be found online at https://doi.org/10.1016/j.electacta.2026.148494.

Data availability

Data will be made available on request.

References

[1] O.A. El-Shafie, R.M. El-Maghraby, J. Albo, S.-E.K. Fateen, A. Abdelghany, Modeling and numerical investigation of the performance of gas diffusion electrodes for the electrochemical reduction of carbon dioxide to methanol, Ind. Eng. Chem. Res. 59 (47) (2020) 20929–20942.
[2] N. Gupta, M. Gattrell, B. MacDougall, Calculation for the cathode surface concentrations in the electrochemical reduction of CO2 in KHCO3 solutions, J. Appl. Electrochem. 36 (2) (2006) 161–172.
[3] L. Jourdin, T. Burdyny, Microbial electrosynthesis: where do we go from here? Trends Biotechnol. 39 (4) (2021) 359–369.
[4] A. Prévoteau, J.M. Carvajal-Arroyo, R. Ganigué, K. Rabaey, Microbial electrosynthesis from CO2: forever a promise? Curr. Opin. Biotechnol. 62 (2020) 48–57.
[5] P. Batlle-Vilanova, R. Ganigué, S. Ramió-Pujol, L. Bañeras, G. Jiménez, M. Hidalgo, M.D. Balaguer, J. Colprim, S. Puig, Microbial electrosynthesis of butyrate from carbon dioxide: Production and extraction, Bioelectrochemistry 117 (2017) 57–64.
[6] F. Matemadombo, S. Puig, R. Ganigué, R. Ramírez-García, P. Batlle-Vilanova, M. Dolors Balaguer, J. Colprim, Modelling the simultaneous production and separation of acetic acid from CO2 using an anion exchange membrane microbial electrosynthesis system, J. Chem. Technol. Biotechnol. 92 (6) (2017) 1211–1217.
[7] P. Dessì, L. Rovira-Alsina, C. Sánchez, G.K. Dinesh, W. Tong, P. Chatterjee, M. Tedesco, P. Farràs, H.M. Hamelers, S. Puig, Microbial electrosynthesis: towards sustainable biorefineries for production of green chemicals from CO2 emissions, Biotech. Adv. 46 (2021) 107675.
[8] S. Bajracharya, S. Srikanth, G. Mohanakrishna, R. Zacharia, D.P. Strik, D. Pant, Biotransformation of carbon dioxide in bioelectrochemical systems: State of the art and future prospects, J. Power Sources 356 (2017) 256–273.
[9] Y.E. Song, A. Mohamed, C. Kim, M. Kim, S. Li, E. Sundstrom, H. Beyenal, J.R. Kim, Biofilm matrix and artificial mediator for efficient electron transport in CO2 microbial electrosynthesis, Chem. Eng. J. 427 (2022) 131885.
[10] L. Jourdin, D. Strik, Electrodes for cathodic microbial electrosynthesis processes: key-developments and criteria for effective research & implementation, Funct. Electrodes Enzym. Microb. Bioelectrochemical Syst. (2017) 429–473.
[11] S. Kerzenmacher, Engineering of microbial electrodes, Bioelectrosynthesis (2019) 135–180.
[12] K. Nevin, T. Woodard, A. Franks, Z. Summers, D. Lovley, R. Colwell, Microbial electrosynthesis: feeding microbes electricity to convert carbon dioxide and water to multicarbon extracellular organic compounds, mBio 1 (2)(2010), View Scopus (2010) 00103–00110.
[13] O. Cabau-Peinado, A.J. Straathof, L. Jourdin, A general model for biofilm-driven microbial electrosynthesis of carboxylates from CO2, Front. Microbiol. 12 (2021) 669218.
[14] S. Tian, H. Wang, Z. Dong, Y. Yang, H. Yuan, Q. Huang, T.-s. Song, J. Xie, Mo 2 C-induced hydrogen production enhances microbial electrosynthesis of acetate from CO 2 reduction, Biotechnol. Biofuels 12 (2019) 1–12.
[15] Y. Jiang, H.D. May, L. Lu, P. Liang, X. Huang, Z.J. Ren, Carbon dioxide and organic waste valorization by microbial electrosynthesis and electro-fermentation, Water Res. 149 (2019) 42–55.
[16] B. Korth, F. Harnisch, Modeling microbial electrosynthesis, Bioelectrosynthesis (2019) 273–325.
[17] M. Kazemi, D. Biria, H. Rismani-Yazdi, Modelling bio-electrosynthesis in a reverse microbial fuel cell to produce acetate from CO2 and H2O, Phys. Chem. Chem. Phys. 17 (19) (2015) 12561–12574.
[18] S. Gadkari, M. Shemfe, J.A. Modestra, S.V. Mohan, J. Sadhukhan, Understanding the interdependence of operating parameters in microbial electrosynthesis: a numerical investigation, Phys. Chem. Chem. Phys. 21 (20) (2019) 10761–10772.
[19] M. Kim, J. Yoo, M. Kim, J.H. Kim, Y. Lee, H. Lee, H.-i. Kim, J. Jae, J.R. Kim, S.H. Son, Fundamental modeling of microbial electrosynthesis system using porous electrodes for CO2-to-acetate conversion, Bioresour. Technol. 424 (2025) 132154.
[20] Z. Li, Q. Fu, H. Chen, S. Xiao, J. Li, Q. Liao, X. Zhu, A mathematical model for CO2 conversion of CH4-producing biocathodes in microbial electrosynthesis systems, Renew. Energy 183 (2022) 719–728.
[21] R. Gharbi, A.G. Vidales, S. Omanovic, B. Tartakovsky, Mathematical model of a microbial electrosynthesis cell for the conversion of carbon dioxide into methane and acetate, J. CO2 Util. 59 (2022) 101956.
[22] C. Quintela, P. Bountzis, B. Rezaei, C. Im, O. Modin, Y. Nygård, L. Olsson, I.V. Skiadas, H.N. Gavala, Chain elongation in continuous microbial electrosynthesis cells: The effect of pH and precursors supply, J. CO2 Util. 83 (2024) 102789.
[23] L. Jourdin, M. Winkelhorst, B. Rawls, C.J. Buisman, D.P. Strik, Enhanced selectivity to butyrate and caproate above acetate in continuous bioelectrochemical chain elongation from CO2: steering with CO2 loading rate and hydraulic retention time, Bioresour. Technol. Rep. 7 (2019) 100284.
[24] S. Bajracharya, A. ter Heijne, X.D. Benetton, K. Vanbroekhoven, C.J. Buisman, D.P. Strik, D. Pant, Carbon dioxide reduction by mixed and pure cultures in microbial electrosynthesis using an assembly of graphite felt and stainless steel as a cathode, Bioresour. Technol. 195 (2015) 14–24.
[25] R. Ganigué, S. Puig, P. Batlle-Vilanova, M.D. Balaguer, J. Colprim, Microbial electrosynthesis of butyrate from carbon dioxide, Chem. Commun. 51 (15) (2015) 3235–3238.
[26] J. Madjarov, R. Soares, C.M. Paquete, R.O. Louro, Sporomusa ovata as catalyst for bioelectrochemical carbon dioxide reduction: a review across disciplines from microbiology to process engineering, Front. Microbiol. 13 (2022) 913311.
[27] L. Muñoz-Duarte, S. Chakraborty, L.V. Grøn, M.F. Bambace, J. Catalano, J. Philips, H2 consumption by various acetogenic bacteria follows first-order kinetics up to H2 saturation, Biotechnol. Bioeng. 122 (4) (2025) 804–816.
[28] Z. Liu, X. Xue, W. Cai, K. Cui, S.A. Patil, K. Guo, Recent progress on microbial electrosynthesis reactor designs and strategies to enhance the reactor performance, Biochem. Eng. J. 190 (2023) 108745.
[29] S.W. Ragsdale, E. Pierce, Acetogenesis and the Wood–Ljungdahl pathway of CO2 fixation, Biochim. Biophys. Acta (BBA)-Proteins Proteom. 1784 (12) (2008) 1873–1898.
[30] N. Chu, W. Hao, Q. Wu, Q. Liang, Y. Jiang, P. Liang, Z.J. Ren, R.J. Zeng, Microbial electrosynthesis for producing medium chain fatty acids, Engineering 16 (2022) 141–153.
[31] B.E. Logan, R. Rossi, A. Ragab, P.E. Saikaly, Electroactive microorganisms in bioelectrochemical systems, Nat. Rev. Microbiol. 17 (5) (2019) 307–319.
[32] M. Laura, P. Jo, No acetogen is equal: Strongly different H2 thresholds reflect diverse bioenergetics in acetogenic bacteria, Environ. Microbiol. 25 (10) (2023) 2032–2040.
[33] S.M. Raes, L. Jourdin, C.J. Buisman, D.P. Strik, Continuous long-term bioelectrochemical chain elongation to butyrate, ChemElectroChem 4 (2) (2017) 386–395.
[34] I. Vassilev, P.A. Hernandez, P. Batlle-Vilanova, S. Freguia, J.O. Krömer, J. Keller, P. Ledezma, B. Virdis, Microbial electrosynthesis of isobutyric, butyric, caproic acids, and corresponding alcohols from carbon dioxide, ACS Sustain. Chem. Eng. 6 (7) (2018) 8485–8493.
[35] K. Zhang, Z. Qiu, D. Luo, T. Song, J. Xie, Hybrid electron donors of ethanol and lactate stimulation chain elongation in microbial electrosynthesis with different inoculants, Renew. Energy 202 (2023) 942–951.
[36] B. Korth, L.F. Rosa, F. Harnisch, C. Picioreanu, A framework for modeling electroactive microbial biofilms performing direct electron transfer, Bioelectrochemistry 106 (2015) 194–206.
[37] R. González-Cabaleiro, J.M. Lema, J. Rodríguez, R. Kleerebezem, Linking thermodynamics and kinetics to assess pathway reversibility in anaerobic bioprocesses, Energy Environ. Sci. 6 (12) (2013) 3780–3789.
[38] A. Lasia, Mechanism and kinetics of the hydrogen evolution reaction, Int. J. Hydrog. Energy 44 (36) (2019) 19484–19518.
[39] M. Chatenet, B.G. Pollet, D.R. Dekel, F. Dionigi, J. Deseure, P. Millet, R.D. Braatz, M.Z. Bazant, M. Eikerling, I. Staffell, et al., Water electrolysis: from textbook knowledge to the latest scientific strategies and industrial developments, Chem. Soc. Rev. 51 (11) (2022) 4583–4762.
[40] S. Anantharaj, S. Noda, Amorphous catalysts and electrochemical water splitting: an untold story of harmony, Small 16 (2) (2020) 1905779.
[41] M.d. Galvez-Vazquez, V. Grozovski, N. Kovács, P. Broekmann, S. Vesztergom, Full model for the two-step polarization curves of hydrogen evolution, measured on RDEs in dilute acid solutions, J. Phys. Chem. C 124 (7) (2020) 3988–4000.
[42] K. Obata, L. Stegenburga, K. Takanabe, Maximizing hydrogen evolution performance on pt in buffered solutions: Mass transfer constrains of H2 and buffer ions, J. Phys. Chem. C 123 (35) (2019) 21554–21563.

[43] Z. Zhou, Z. Pei, L. Wei, S. Zhao, X. Jian, Y. Chen, Electrocatalytic hydrogen evolution under neutral pH conditions: current understandings, recent advances, and future prospects, Energy Environ. Sci. 13 (10) (2020) 3185–3206.
[44] I. Katsounaros, J.C. Meier, S.O. Klemm, A.A. Topalov, P.U. Biedermann, M. Auinger, K.J. Mayrhofer, The effective surface pH during reactions at the solid–liquid interface, Electrochem. Commun. 13 (6) (2011) 634–637.
[45] M. Auinger, I. Katsounaros, J.C. Meier, S.O. Klemm, P.U. Biedermann, A.A. Topalov, M. Rohwerder, K.J. Mayrhofer, Near-surface ion distribution and buffer effects during electrochemical reactions, Phys. Chem. Chem. Phys. 13 (36) (2011) 16384–16394.
[46] T. Shinagawa, A.T. Garcia-Esparza, K. Takanabe, Insight on tafel slopes from a microkinetic analysis of aqueous electrocatalysis for energy conversion, Sci. Rep. 5 (1) (2015) 13801.
[47] V. Grozovski, S. Vesztergom, G.G. Láng, P. Broekmann, Electrochemical hydrogen evolution: H+ or H2O reduction? A rotating disk electrode study, J. Electrochem. Soc. 164 (11) (2017) E3171.
[48] C. Picioreanu, M.C. van Loosdrecht, T.P. Curtis, K. Scott, Model based evaluation of the effect of pH and electrode geometry on microbial fuel cell performance, Bioelectrochemistry 78 (1) (2010) 8–24.
[49] S. Ou, H. Kashima, D.S. Aaron, J.M. Regan, M.M. Mench, Full cell simulation and the evaluation of the buffer system on air-cathode microbial fuel cell, J. Power Sources 347 (2017) 159–169.
[50] R.B. Bird, Transport phenomena, Appl. Mech. Rev. 55 (1) (2002) R1–R4.
[51] H. Beyenal, Z. Lewandowski, Internal and external mass transfer in biofilms grown at various flow velocities, Biotechnol. Prog. 18 (1) (2002) 55–61.
[52] H. Horn, D.C. Hempel, Substrate utilization and mass transfer in an autotrophic biofilm system: experimental results and numerical simulation, Biotechnol. Bioeng. 53 (4) (1997) 363–371.
[53] H. Horn, D.C. Hempel, Modeling mass transfer and substrate utilization in the boundary layer of biofilm systems, Water Sci. Technol. 37 (4–5) (1998) 139–147.
[54] V. Gogulancea, R. González-Cabaleiro, B. Li, D. Taniguchi, P.G. Jayathilake, J. Chen, D. Wilkinson, D. Swailes, A.S. McGough, P. Zuliani, et al., Individual based model links thermodynamics, chemical speciation and environmental conditions to microbial growth, Front. Microbiol. 10 (2019) 1871.
[55] A. De Lichtervelde, A. Ter Heijne, H. Hamelers, P. Biesheuvel, J. Dykstra, Theory of ion and electron transport coupled with biochemical conversions in an electroactive biofilm, Phys. Rev. Appl. 12 (1) (2019) 014018.
[56] A.K. Marcus, C.I. Torres, B.E. Rittmann, Analysis of a microbial electrochemical cell using the proton condition in biofilm (PCBIOFILM) model, Bioresour. Technol. 102 (1) (2011) 253–262.